

Cooperative Interactions between Surface Terminations Explain Photocatalytic Water Splitting Activity on SrTiO₃

Vidushi Sharma^{1,2,3,4,*} Benjamin Bein³ Amanda Lai,³ Betül Pamuk⁵ Cyrus E. Dreyer^{3,6} Marivi Fernández-Serra^{3,4,†} and Matthew Dawber^{3,‡}

¹Theoretical Division, Los Alamos National Laboratory, Los Alamos, New Mexico 87545, USA

²Center for Nonlinear Studies (CNLS), Los Alamos National Laboratory, Los Alamos, New Mexico 87545, USA

³Department of Physics and Astronomy, Stony Brook University, Stony Brook, New York 11794-3800, USA

⁴Institute for Advanced Computational Science, Stony Brook University, Stony Brook, New York 11794-3800, USA

⁵School of Applied and Engineering Physics, Cornell University, Ithaca, New York 14853, USA

⁶Center for Computational Quantum Physics, Flatiron Institute, 162 5th Avenue, New York, New York 10010, USA



(Received 10 February 2022; revised 23 May 2022; accepted 3 June 2022; published 14 July 2022)

SrTiO₃ is a highly efficient photocatalyst for the overall water splitting reaction under UV irradiation. However, an atomic-level understanding of the active surface sites responsible for the oxidation and reduction reactions is still lacking. Here we present a unified experimental and computational account of the photocatalytic activity at the SrO and TiO₂ terminations of aqueous solvated [001] SrTiO₃. Our experimental findings show that the overall water-splitting reaction proceeds on the SrTiO₃ surface only when the two terminations are simultaneously exposed to water. Our simulations explain this, showing that the photogenerated hole-driven oxidation primarily occurs at SrO surfaces in a sequence of four single hole transfer reactions, while the TiO₂ termination effects the crucial band alignment of the photocatalyst relative to the water oxidation potential. The present work elucidates the interdependence of the two chemical terminations of SrTiO₃ surfaces, and has consequent implications for maximizing sustainable solar-driven water splitting.

DOI: [10.1103/PRXEnergy.1.023002](https://doi.org/10.1103/PRXEnergy.1.023002)

I. INTRODUCTION

Photocatalytic water splitting is a promising route to decrease our energy dependence on fossil fuels [1,2]. Redox-active oxides like TiO₂ are ideal material platforms to study and optimize the heterogeneous oxidation and reduction reactions to convert water into H₂ and O₂ using solar photons as the sole source of energy [3–6]. Some of the best photocatalysts are oxide materials [7,8] and specifically perovskite oxides [9]. Perovskite oxide materials have the ability to selectively separate the photogenerated electrons and holes and efficiently transfer them to the semiconductor surfaces, where they can drive the two redox half reactions [10].

SrTiO₃ is a prototypical cubic perovskite and was first proposed as a photocatalyst for water splitting to generate hydrogen in 1976 [11]. Despite having a band gap of 3.25 eV [12] that restricts the photons absorbed to the ultraviolet range of the solar spectrum, SrTiO₃ is a well-studied photoreactive material and serves as a platform for understanding photocatalytic water splitting in more complex systems [11,13–25]. Many different factors influencing the quantum efficiency of SrTiO₃ have been investigated. These include, for example, the effects of doping [26–28], the influence of different facets [14,29], and the effects of the pH of the solution [30,31]. However, a complete microscopic picture of the photocatalytic process, even in this model system, is missing. A significant reason for this is that many aspects of the process depend on the details of the SrTiO₃ surface, and its aqueous interface. Considerable work has been performed in recent years on understanding the photocatalytic nature of these surfaces [13,29,30,32,33], but far less is known about the atomistic details of the oxidation mechanism at the aqueous interface [34]. This is in part due to a lack of experimental data obtained from samples designed with controlled surface properties. Such information will be critical for integrating theoretical models and experiments in a unified study [8].

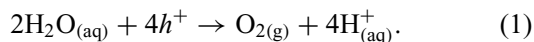
*vidushi@lanl.gov

†maria.fernandez-serra@stonybrook.edu

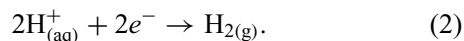
‡matthew.dawber@stonybrook.edu

Published by the American Physical Society under the terms of the [Creative Commons Attribution 4.0 International license](https://creativecommons.org/licenses/by/4.0/). Further distribution of this work must maintain attribution to the author(s) and the published article's title, journal citation, and DOI.

The oxidation reaction of water to molecular oxygen is a complicated four-electron reaction, coupled to the reduction of water into molecular hydrogen. In heterogeneous photocatalysis, the photogenerated holes drive the water oxidation at the semiconductor surface:



In an overall water-splitting material, the hydrogen production or proton reduction also occurs at the surface:



The two half reactions need to proceed at the same rate, as otherwise, the full redox reaction will be shut down by charge accumulation. Therefore, among the factors limiting the quantum efficiency, charge separation is a dominant one [10,29,30,35]. This implies that the photogenerated electron-hole pairs, which in SrTiO₃ usually exist in the form of a self-trapped exciton or separated electron and hole polarons [36], need to arrive at their corresponding surface reaction active sites at similar rates in order to maximize the efficiency of the overall water-splitting reaction. This idea has been proposed previously by Zhang *et al.* [30], in their study of photochemical reactivity at different SrTiO₃ surfaces.

In this work, we identify the explicit roles that surface chemistry and termination have in the overall water-splitting reaction in SrTiO₃ [001] surfaces, using a combination of experimental and computational approaches. Crucially, our surface treatment techniques allow us to deterministically produce samples with either only an SrO termination, only a TiO₂ termination, or a mixture of both.

To experimentally evaluate the redox reaction, we replace Eq. (2) by the reduction of an electron scavenger. Specifically, we observe the reduction of Ag⁺ into metallic Ag; thus, the detection of metallic Ag at the surface of the semiconductor serves as a proxy for the evaluation of the efficiency of the overall redox reaction [13,30,32]. These experiments demonstrate that SrTiO₃ is only photocatalytically active if *both* SrO and TiO₂ terminations are present on the surface. A microscopic explanation for this result is given by *ab initio* molecular dynamics simulations of water atop an SrTiO₃ slab with the two relevant surfaces exposed to water. In addition to providing a clear atomistic description of these interfaces, the simulation results allow us to evaluate and propose a model for the oxidation reaction at the surface that explains the experimental results. Furthermore, the combined results provide information on the nature of the photoexcited carriers, by identifying the spatial correlation between the oxidation and reduction sites at the surfaces.

II. PHOTOCATALYSIS ON ENGINEERED SrTiO₃ [001] SURFACES

The focus of this work is characterizing photocatalysis on the [001] surfaces of SrTiO₃. Along the (001) direction the material can be viewed as a stack of alternating TiO₂ and SrO planes, and [001] surfaces can be terminated in either of these two planes. Practically, all substrates cut from a crystal will have a small miscut angle so that the surface will not be an exact [001] plane. In the absence of further treatments, the surface of a substrate that has been cut and polished will present a mixture of the two possible terminations. However, there are procedures to obtain atomically flat surfaces with a well-defined step and terrace structure, typically used as preparation for the growth of epitaxial thin films [37–39]. We leverage these techniques to provide a controlled surface for the study of photocatalysis.

The substrate vendor (Cyrstec) provided us with two types of substrates: (i) untreated substrates, which are just cut and polished and (ii) single termination substrates that had been treated to achieve a TiO₂ termination [38,40,41]. Untreated substrates were subsequently etched, via high-temperature high-pressure water etching [42]. The etching process takes place within a microwave acid digestion vessel (model 4782 from Parr), a machined polytetrafluoroethylene cup sealed within a high-strength, microwave-transparent polymer. The vessel is filled with 20 mL distilled water and the substrate and placed in a Panasonic NN-SN651B inverter microwave oven at power level 3 of 10, for 4 min. Etching is followed by annealing in air inside an insulating box on top a MeiVac 2.0 in. high-temperature resistive substrate heater. The water etching method has an advantage over treatments that involve buffered HF in that it avoids F[−] impurities that can be introduced by traditional buffered hydrofluoric acid etching [43]. The water treatment leads to mostly pure TiO₂ surfaces with patches of SrO. Subsequent annealing can then be used to modify the SrO coverage of the substrates [44].

Photocatalytic activity on all surfaces is evaluated using the Ag⁺ proxy reduction method for water splitting developed in Refs. [1,13,14,45]. Each sample is placed in 0.002 mol AgNO₃ solution and illuminated with a 100 W mercury vapor lamp at a distance of 60 cm for 5 min. A UV fused silica ground glass diffuser is placed in front of the sample (Edmund Optics NT49-159). Upon UV illumination, water is oxidized to O₂ and H⁺ [see Eq. (1)] while the reduction of H⁺ [Eq. (2)] is replaced with the reduction of Ag⁺ ions, resulting in Ag deposited on the surface. The photocatalytically deposited silver can then be observed using atomic force microscopy (AFM). When this experiment is performed on an untreated surface [left scan of Fig. 1(a)], the silver appears to be deposited fairly uniformly [right scan of Fig. 1(a)], with no particular order visible. The left scan of Fig. 1(b) shows a sample that

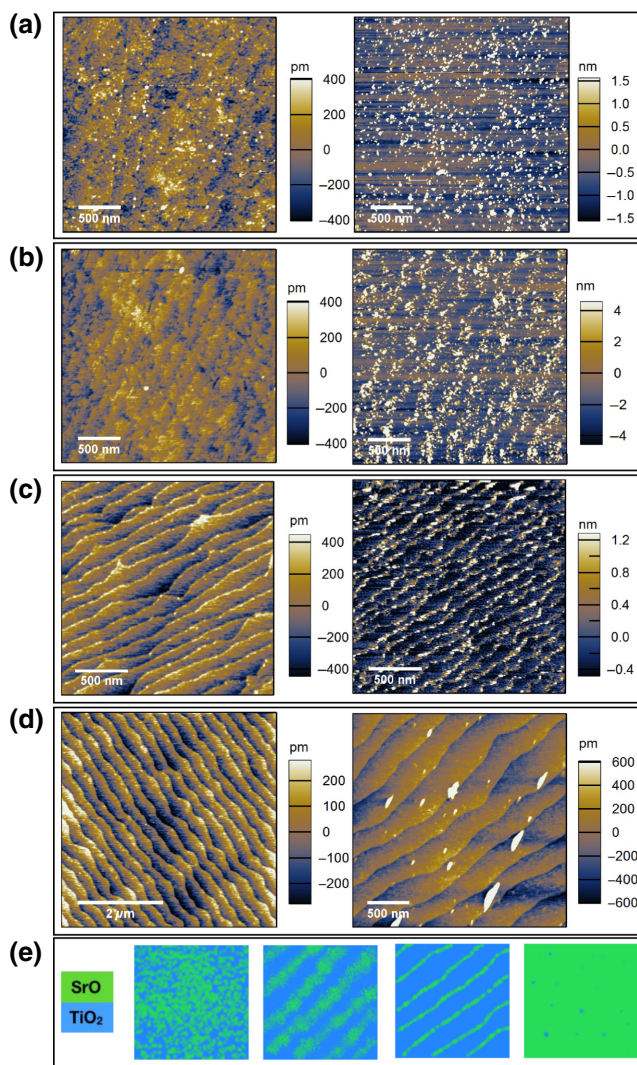


FIG. 1. AFM topography scans of surfaces before (left) and after (right) silver deposition. (a) SrTiO₃ surface that has been cut and polished only, (b) surface that has been treated with a procedure that only partially segregates the SrO on the surface, (c) surface that has been treated such that SrO is segregated to the step edges, (d) surface that has been treated to obtain SrO termination by extending the duration of the high-temperature anneal. Panel (e) shows (from left to right) artistic representations of the termination arrangement corresponding to (a)–(d).

is treated using a high-pressure water etch, annealed at 650 °C for 24 h, retreated, and then annealed again for 24 h at 750 °C. The step near-edges are now visible in the etched sample, but are not very straight. The thermal treatment of this sample has led to residual SrO starting to diffuse towards the step edges. Photocatalyzed silver deposition appears to be associated with the residual SrO, as observed in the right scan of Fig. 1(b).

That Ag deposition indeed occurs in the vicinity of SrO patches is more evident in our next treated sample shown in Fig. 1(c). This sample is obtained after adding

an additional 2 h anneal at 900 °C. This results in the SrO completing its diffusion along the TiO₂ step and collecting on the step near-edge as a 1/2 unit-cell layer [left scan of Fig. 1(c)]. This is most obvious in a line profile taken perpendicular to the step edges [Fig. 2(a)]. Here it can be seen that there is a 0.6 nm jump at each step edge that corresponds to 1.5 unit-cell steps; the change from SrO to TiO₂ termination happens with a 0.2 nm drop that corresponds to 0.5 unit-cell steps. The 0.5 unit-cell high region of SrO termination has a finite spatial extent, as seen from the line plot, its width extends to 20–50 nm from the beginning of the terrace and so they are best thought of as “near-edge” regions. The preference of SrO to segregate along the step edges is a known property [46] and a similar surface was previously achieved by Bachelet *et al.*, albeit with a different heat treatment [44,47]. After photoreactivity on this surface, the silver is clearly found in the vicinity of the step edges where the SrO has collected [see Figs. 1(c) and 2(a)].

A fully SrO-terminated surface can be obtained by replacing the anneal after the second treatment with a sustained high-temperature anneal (38 h at 900 °C). This extended high-temperature anneal causes SrO to vertically diffuse from the bulk of the sample [46] and produces a highly ordered single termination SrO surface [left scan of Fig. 1(d)]. Of course, a prerequisite for obtaining this highly ordered SrO surface is that prior to the high-temperature anneal, the surface is actually single termination TiO₂ so that SrO can freely diffuse on the surface towards the step edge. Further information showing some of the intermediate steps in the treatment procedure can be found in Fig. S10 within the Supplemental Material [48]. As shown in Fig. 2(b), this surface has single unit-cell transitions at the step edges. Remarkably, as observed in the right scan of Fig. 1(d), very little silver is deposited on this

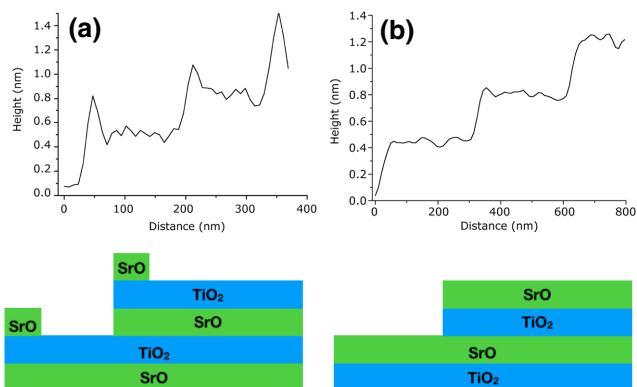


FIG. 2. AFM line profiles perpendicular to step edges. (a) Line profile of a surface that has been treated such that SrO is segregated to the step edges. (b) Line profile of a surface that has been treated to obtain SrO termination. Bottom figures illustrate the distribution of SrO and TiO₂ planes corresponding to the line profiles.

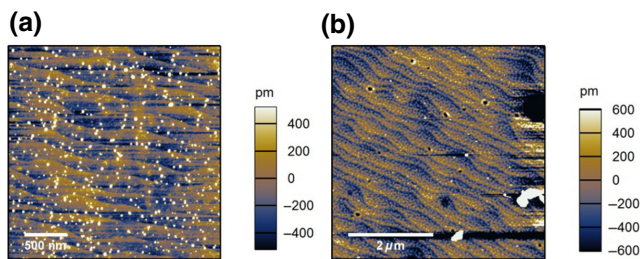


FIG. 3. AFM topography scans of TiO_2 -terminated surfaces after silver deposition on (a) a treated substrate and (b) a deposited SrTiO_3 film.

surface, indicating that a pure SrO surface is not photocatalytically active. Most likely the small deposits of Ag observed are associated with tiny regions of the surface that have TiO_2 termination or are related to other structural defects.

We also carry out the silver deposition procedure on two TiO_2 -terminated surfaces. The first is on a TiO_2 substrate treated by the vendor with a buffered HF etch and high-temperature anneal. Here we observe some silver being deposited [Fig. 3(a)], but there is no apparent correlation between the deposition sites and the surface morphology of the film. We associate this small amount of Ag deposited to the presence of F^- impurities at the surface.

For the second surface, we grow SrTiO_3 thin films using an off-axis rf magnetron sputtering on top of vendor- SrTiO_3 substrates with TiO_2 termination. It is expected that these films will maintain a TiO_2 termination. A 35 W power is applied to the 1.3 in. sputter gun. During the growth an atmosphere of 0.24 mbar with an oxygen-to-argon ratio of 7/16 is maintained and the sample is kept at an elevated temperature of 560°C . After performing a photocatalytic silver deposition, very few silver particles are formed on these surfaces, even if we extend the exposure time to 1 h, as shown in Fig. 3(b).

Hence, our experiments show that (i) single terminated surfaces (SrO or TiO_2) are not photocatalytically active, and (ii) mixed terminated surfaces are active, and Ag is deposited near SrO terminations.

III. ATOMISTIC STRUCTURE OF SOLVATED SrTiO_3 (001) SURFACES

In order to obtain an atomistic picture of the photocatalytic process, we perform *ab initio* molecular dynamics simulations of an SrTiO_3 slab in the presence of liquid water. The slab is three unit cells along the (001) direction and $2\sqrt{2} \times 2\sqrt{2}$ unit cells along the in-plane (110) direction. The (bulk) lattice constant for the SrTiO_3 slab is $a = 3.909 \text{ \AA}$. Since we choose to have the slab contain an integer number of unit cells, it is necessarily terminated by an SrO surface on one side, and a TiO_2 surface on the other. This choice allows us to explore in one single simulation

the structure of the two different terminations. We add 64 water molecules between the periodically repeated slabs, which are enough to screen the two different potential offsets arising from this asymmetric slab.

A. DFT simulations and molecular dynamics

The density functional theory- (DFT) based *ab initio* molecular dynamics simulations are performed using the SIESTA code with a Generalized Gradient Approximate (GGA) exchange-correlation functional. Specifically, the vdW-BH functional is used, which includes dispersive corrections for the van der Waals interactions in the system. A double-zeta polarized basis set is used for the electronic wavefunctions of Sr and Ti, while the O orbitals are described using a long-range quadruple-zeta basis set. The size of the oxygen basis set is found to have a significant effect on the band-edge positions as the valence band edge mostly consists of O $2p$ bands; see Table S1 within the Supplemental Material [48].

The interfacial properties and structure of aqueous SrTiO_3 surfaces are analyzed with the help of DFT-based molecular dynamics (MD) simulations. Unlike the case of SrTiO_3 /vacuum symmetric interfaces, in the fully solvated $\text{SrTiO}_3/\text{H}_2\text{O}$ system, water makes contact with two different chemical terminations ($\text{SrO}/\text{H}_2\text{O}$ and $\text{TiO}_2/\text{H}_2\text{O}$) at once; see Fig. 4(a). In our MD simulations of the solvated SrTiO_3 system, the SrTiO_3 slab comprised three layers each of SrO and TiO_2 . The SrO and TiO_2 terminations are separated by about an 18 \AA region of water. Based on the (planar-averaged) macroscopic electrostatic potential of the solvated system, it is confirmed that the water region screens the two asymmetric-terminated surfaces and that there is no net charge transfer from one surface to the other; see Fig. S3 within the Supplemental Material [48].

At the beginning of the MD simulation, the surfaces are nonhydroxylated (no water dissociation). A GGA-type vdW-BH functional is used in SIESTA to perform a 20-ps-long MD simulation with a time step of 0.5 fs. During this MD, the hydrated slab is annealed to a temperature of $T = 330 \text{ K}$ using a velocity rescaling thermostat, and water interacts with the TiO_2 surface on one side and SrO on the other, giving different amounts of dissociation on both sides. Figure 4 shows a snapshot of the simulated system. The two surfaces quickly dissociate water and achieve an equilibrium state within 10 ps of simulation. Experimentally, the presence of OH^- at the [001] SrTiO_3 surface has been thoroughly studied by Domingo *et al.* [49].

As seen in Fig. 4(c), the two surface terminations are active in dissociating water into OH^- (which binds to Sr or Ti depending on the surface termination) and H^+ (which always binds to surface O atoms). However, the SrO -terminated surface is more effective than TiO_2 in this task. Of the water molecules adsorbed at SrO , 35% are dissociated, versus only 25% dissociation of the adsorbed

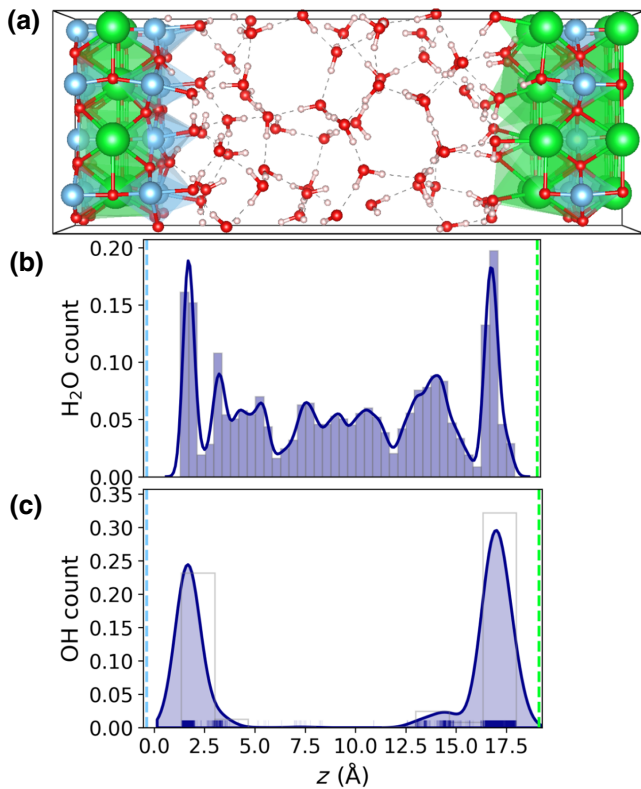


FIG. 4. An equilibrated molecular dynamics simulation for (a) (001) SrTiO₃ surfaces—TiO₂ (left, in blue) and SrO (right, in green)—interacting with a box of 64 water molecules. The number density distribution along the vertical z direction for (b) H₂O molecules and (c) dissociated OH⁻ species. The positions of the TiO₂ and SrO surfaces with respect to the box of water are shown with blue and green dashed lines, respectively.

water molecules seen at TiO₂, implying a higher dissociation event count on SrO. In addition, we observe secondary dissociation events at the SrO surface, which cause the additional peak shoulder in Fig. 4(c) (right). These are transient proton transfer reactions between surface OH⁻ and nearby H₂O molecules, indicating that this surface has a lower pK_a or higher surface acidity [50] than a TiO₂ termination.

IV. ELECTRONIC STRUCTURE AND BAND ALIGNMENT

Among the many factors that control the photocatalytic efficiency of a semiconductor surface, the relative alignment of the semiconductor band edge and the corresponding redox level in water determines whether the photoexcited carriers can carry the oxidation and reduction reactions. In our case, the reduction half reaction is bypassed by the reduction of Ag⁺ and we seek to understand the oxidation reaction, and in particular, its dependence on the semiconductor surface termination. To this end, we must obtain the alignment of the valence band

edge (VBE) with respect to the electrochemical water oxidation potential [34,51] for each surface termination. In oxide perovskites (ABO₃), the work function difference between the AO- and BO₂-terminated (001) surfaces is theoretically predicted to be on the scale of a few electronvolts [52,53]. While the specific case of pure SrTiO₃ has been studied in detail using DFT-based methods [54–56], the aqueous interface band alignment remains unexplored. Here we evaluate the electronic structure on samples of the previously described SrTiO₃ slab, after dissociation at the two water exposed surfaces reaches equilibrium.

In the procedure proposed by Kharche *et al.* [51], the alignment with respect to vacuum for the solvated slab is done using the $1b_1$ level of the bulk water region of the simulated system as a reference. This level is itself aligned with the $1b_1$ level obtained from an independent water-vacuum slab calculation. In Fig. 5, we present the vacuum-aligned band-edge positions of a fully solvated asymmetric SrTiO₃ slab using a hybrid functional HSE06 [57,58]. The first two columns show the band edges of pure SrO- and TiO₂-terminated surfaces with respect to vacuum, as reported by Ma *et al.* [54], which we use as a reference for nonsolvated systems. Additional calculations and discussion about the dependence of the results on the choice of the exchange and correlation functional are presented in Appendix A and the Supplemental Material [48]. The water redox potentials are shown as red dotted lines. As seen in this figure, a pure SrO surface is not favorable for water splitting, given that the corresponding VBE is less positive (that is, closer to vacuum) than the water oxidation potential by about 1.5 eV. On the other hand, pure TiO₂ surfaces present a VBE sufficiently positive to catalyze the water oxidation reaction, albeit with a small, about 0.3 eV, overpotential [54].

The fully solvated SrTiO₃ slab used to compute the alignment in Fig. 5 has one of each, i.e., SrO and TiO₂ surfaces exposed to water. Hence we refer to this system as a 50% mixed surface slab. Although in vacuum each surface has a different work function, in aqueous solution, the surface water screens completely and within a very short distance (less than 5 Å) the surface dipole due to the other termination, as further discussed in the Supplemental Material [48]. As a result of the screening that takes place through both dissociation and structural orientation, the band bending at the two surfaces results in more positive VBES, placing them both about 0.85 eV below the water oxidation potential.

These results indicate that water dissociation, which induces a negative dipole moment (i.e., pointing into the surface), helps with the favorable level alignment for the overall water oxidation reaction at SrTiO₃ surfaces. However, the computed energy alignment upon solvation, which places the VBE of the solvated 50% termination slab 2.3 eV below that of the pure SrO unsolvated slab cannot be explained by the induced water screening dipole alone.

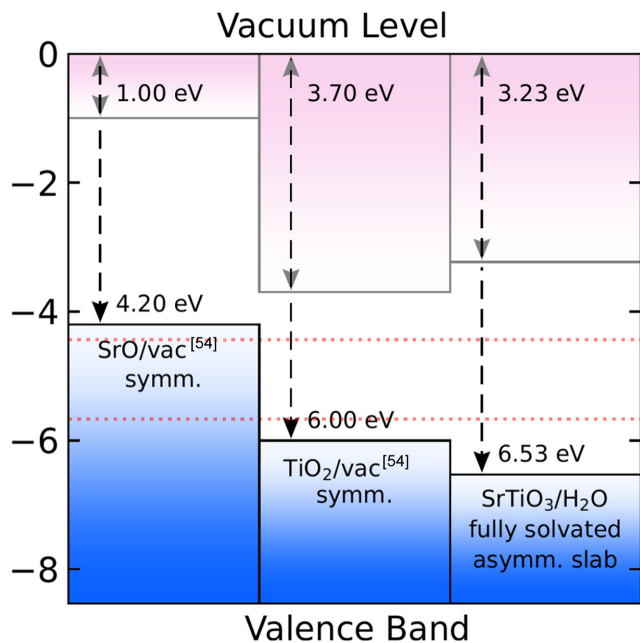


FIG. 5. Band alignments for symmetric SrO-terminated and symmetric TiO₂-terminated SrTiO₃/vacuum as reported in Ref. [54], and fully solvated SrTiO₃/H₂O slabs using DFT HSE06. The red dotted lines indicate the water redox potentials referenced to the vacuum level ($E_{\text{H}^+/\text{H}_2} = -4.44$ eV, $E_{\text{O}_2/\text{H}_2\text{O}} = -5.67$ eV).

It was previously observed in Ref. [51] that this screening could account for an energy lowering of at most 0.5–1.0 eV. In order to achieve an energy alignment sufficient to drive the oxidation reaction, it is also necessary for both terminations to be present at the surface. This is because the surface dipole of SrO-terminated surfaces is coupled to the corresponding dipole of TiO₂ terminations. The overall VBE lowering will depend on the ratio of one termination to another. Our simulation results are obtained for a 50% ratio, but for different ratios, some bowing should be expected [59]. This is why pure SrO surfaces cannot drive the oxidation reaction and hence no Ag deposition is observed in the experiments. However, these results are still not adequate to explain why pure TiO₂ surfaces are not photocatalytically active, nor do they explain why Ag is deposited at or near SrO terminations. To this end, we augment our theoretical study with additional insights about the water oxidation reaction.

V. PHOTOCATALYTIC WATER OXIDATION REACTIONS

Water oxidation on semiconducting surfaces can occur via a sequential four-step proton-coupled electron transfer (PCET) mechanism [34,60]. Here we compute the free energy changes of four PCET reactions both at the SrO/water and TiO₂/water interfaces. The proposed cycle

intermediates match the homogeneous reactions for water oxidation in aqueous solutions. At each of these steps, an incident UV photon generates an electron-hole pair. The resulting hole participates in the oxidation of water at an active surface site. These reactions are coupled to the reduction of four Ag⁺ ions at the surface by the corresponding electrons.

Our proposed four-step PCET cycle for water oxidation at the SrTiO₃/water interface is shown in Fig. 6(a), where (i)–(v) represent relaxed structures obtained after removing a proton coupled with an electron. The reaction intermediates in the proposed PCET mechanism are identified as: (i) OH[−] (adsorbed at a surface Sr or Ti), (ii) O^{•−} (oxygen anion radical), (iii) OOH[−] (hydroperoxyl radical), (iv) O₂^{•−} (superoxide ion), and (v) OH[−]. Upon removing a proton and an electron from OH[−], an oxygen anion radical is formed in the first step; see Fig. 6(a), (i)→(ii). Since there is no longer a proton available at the active species, a neighboring hydrogen-bonded water molecule is chosen and its proton and electron are removed in the second step, (ii)→(iii). A geometric relaxation leads to a spontaneous O—O bond formation resulting in a OOH[−] species at the site. In the third step (iii)→(iv), an electron and proton are removed from the intermediate OOH[−], which gives rise to a superoxide ion (O₂^{•−}) with a shorter O—O bond distance. As shown in Fig. 6(a)(iv), the superoxide ion does not immediately dissociate from the surface. Thus, in the final step (iv)→(v), a concerted electron-proton transfer from yet another neighboring water molecule results in an OH[−]. This newly formed OH[−] attacks the active site and replaces the superoxide ion that now leaves its surface position as O₂.

We have computed the standard Gibbs free energy changes and the standard one-electron reduction potentials (E°) for two active sites on SrO and three on TiO₂ terminations; see Tables S1 and S2 within the Supplemental Material [48]. Table I shows a comparison of the mean E° for the water oxidation pathway on the two surfaces. The mean distance between the interacting oxygens (d_{OO}) in any given reaction intermediate is also reported. On the SrO-terminated surface, the first step that entails the conversion of OH[−] to O^{•−} is rate limiting and requires the maximum reduction potential (about 2.1 eV). In photocatalytic oxidation, the overpotential is the excess energy carried by the hole. This energy is supplied by the photogenerated holes that carry excess energy supplied from the absorbed photon. This is often taken as the energy of the valence band edge versus the NHE water oxidation potential at $p\text{H} = 0$. As previously shown, our calculations report this energy to be about 0.85 eV for a solvated SrTiO₃ slab with 50% TiO₂/SrO terminations. This is not sufficient for the reaction to proceed. However, the expected overpotential increases with the proportion of TiO₂ at the surface. This explains the experimentally observed majority of surface TiO₂ composition in the photocatalytically

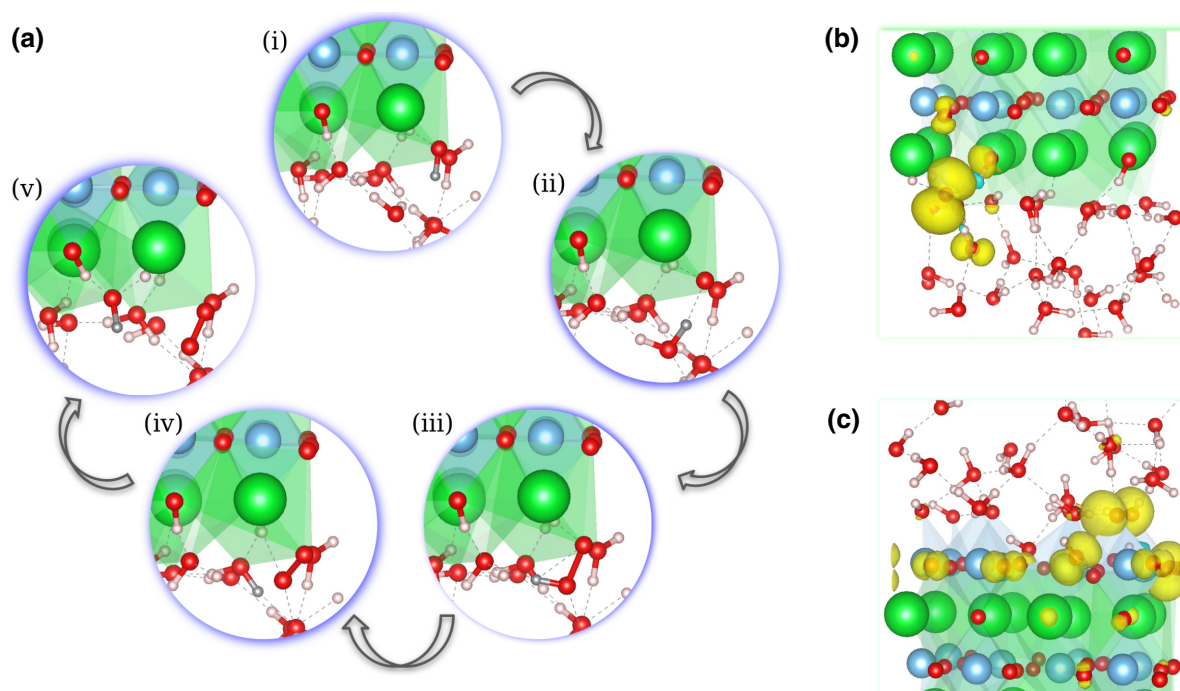


FIG. 6. (a) A sequence of four PCET events reveal the pathway for conversion of (i) $\text{OH}_{\text{adsorbed}}^-$ to (v) O_2 at the SrO surface via three reaction intermediates: (ii) oxygen anion radical ($\text{O}^{\bullet-}$), (iii) hydroperoxyl radical (OOH^-), (iv) superoxide ion ($\text{O}_2^{\bullet-}$). The proton removed at each stage of the PCET mechanism is highlighted in gray. Spin density (in yellow) corresponding to $\text{O}^{\bullet-}$ species formed at (b) SrO-terminated and (c) TiO_2 -terminated aqueous SrTiO_3 surfaces.

active samples. The second step on the SrO surface follows an energetically downhill path, so the formation of OOH^- does not require any energy from the hole. This also suggests that the two-electron process that takes $\text{OH}^- \rightarrow \text{OOH}^-$ directly could be more favorable than the sequential one-electron processes. Interestingly, the presence of the intermediate species proposed here has been observed experimentally in these surfaces, albeit without enough information to identify the two different possible terminations [49]. Table I shows that the net potential for a simultaneous two-electron process is about 1 eV, which makes it energetically accessible for an SrO surface to drive the catalytic cycle with a lower photohole potential.

If we consider the same PCET-based water oxidation mechanism on the TiO_2 surface, the results are rather different. The first step requires a lower potential than the corresponding step on the SrO side. However, the consequent step, that is, the conversion of $\text{O}^{\bullet-}$ to OOH^- , is not supported on the TiO_2 surface. As seen in Table I and in the Supplemental Material [48], this second PCET reaction does not result in an O—O bond (the relaxed O—O distance is 2.3 Å). The reason for the inadequacy of this surface to catalyze the oxidation of the oxygen anion radical is not obvious. Figures 6(b) and 6(c) show the spin density of the radical $\text{O}^{\bullet-}$ state [Fig. 6(a)(ii)] on the SrO (b) and TiO_2 (c) surfaces. While this p_z -like orbital is highly

localized and perpendicular to the SrO surface, on TiO_2 , the orbital is parallel to the surface and much more delocalized within the surface oxygens. Hence, this is a far less reactive species, given that the nearest H_2O molecule needed for the following PCET reaction is oriented along the nodal plane of the $\text{O}^{\bullet-}$ radical electron.

The lack of formation of a crucial intermediate in the PCET mechanism points to an inability of the TiO_2 termination to catalyze the oxidation process. This also explains the lack of reactivity observed on a pure TiO_2 termination by AFM experiments, and further supports the observation that an SrO surface is necessary in conjunction with TiO_2 for the photocatalytic oxidation of water. Our theoretical results clearly indicate that the oxidation reaction proceeds only in SrO-terminated surfaces. Our experiments also show that Ag^+ is reduced at or in the vicinity of these surfaces. Taken together, these results provide indirect information about the nature and localization of the photoexcited carriers. They indicate that both the reduction and oxidation reactions happen in close spatial proximity, and, hence, the exciton does not break before reaching the surface. This is consistent with a previously computed exciton radius of about 5 Bohr radii and a binding energy of 330 eV [61].

It is also worthwhile to comment on the connection to the reduction reaction. While our work does not directly

TABLE I. Calculated standard one- and two-electron reduction potentials for PCET steps at the SrO- and TiO₂-terminated aqueous SrTiO₃ interface. The values are reported with respect to the normal hydrogen electrode (NHE) scale. Roman numerals next to each compound refer to the labeling in Fig. 6. Entries superscripted with a dagger (†) indicate the values for a loosely bound O – OH[−] as the hydroperoxyl radical is *not* formed in this case.

Step	Reaction on SrTiO ₃ termination	SrO plane		TiO ₂ plane	
		E° (eV)	d_{OO} (Å)	E° (eV)	d_{OO} (Å)
1	(ii) *O ^{•−} + H ⁺ + e [−] → (i) *OH [−]	2.123 ± 0.028	(ii) 2.64 ± 0.01	1.85 ± 0.11	(ii) 2.56 ± 0.04
2	(iii) *OOH [−] + H ⁺ + e [−] → (ii) *O ^{•−} + H ₂ O	−0.011 ± 0.008	(iii) 1.483 ± 0.007	1.93 ± 0.02 [†]	(iii) 2.3 ± 0.1 [†]
3	(iv) *O ₂ ^{•−} + H ⁺ + e [−] → (iii) *OOH [−]	0.585 ± 0.107	(iv) 1.353 ± 0.003
4	(v) *OH [−] + O ₂ + H ⁺ + e [−] → (iv) *O ₂ ^{•−} + H ₂ O	0.797 ± 0.184	(v) 1.248 ± 0.003
1 + 2	*OOH [−] + 2H ⁺ + 2e [−] → (i) *OH [−] + H ₂ O	1.049 ± 0.007
3 + 4	O ₂ + *OH [−] + 2H ⁺ + 2e [−] → *OOH [−] + H ₂ O	0.67 ± 0.01

address it, we can conclude that, in principle, this reaction should occur exclusively at TiO₂ terminations. The bottom of the conduction band is mostly composed of Ti 3*d* orbital states (seen in Figs. S3, S4, and S6 within the Supplemental Material [48]); hence, the photoexcited electrons are localized at Ti sites. There is also experimental evidence for the electron migration to these surfaces [62–65]. In our experiments, Ag is deposited on top of the regions of TiO₂ termination, in proximity to regions of SrO termination. This observation supports the picture of a cooperative interaction between the two terminations, such that the exciton has a compact spatial extension on SrTiO₃ [001] surfaces.

VI. CONCLUSIONS

In conclusion, we have presented a combined experimental and computational study of photocatalytic water-splitting activity at SrTiO₃ [001] surfaces. Using the proxy reaction of Ag⁺ to Ag reduction, we have shown that pure SrO or TiO₂ terminations are not photoactive. Ag is only deposited when mixed terminations are present at the surface and deposition occurs near SrO terminations. Our first-principles simulations explain these findings and unambiguously show that water oxidation can only occur at SrO surfaces, which efficiently catalyze a four-hole oxidation cycle. TiO₂ terminations are needed to provide the correct band-energy alignment, but they are unfit to catalyze the necessary surface reactions. These results have important implications for understanding the interplay between surface chemistry and band alignment in semiconductor materials for photocatalytic water splitting. They highlight the importance of achieving a particular surface nanostructure, ideally through bulk synthesis routes or simple chemical-thermal treatments such as those presented in this work. We plan to investigate whether this result can be generalized to other perovskite oxide materials, for which ferroelectricity might provide an additional surface alignment and control handle.

ACKNOWLEDGMENTS

M.D., A.L., and B.B. were supported by NSF DMR-1055413 and DMR-1334867. M.F.-S. and V.S. were funded by the U.S. Department of Energy, Office of Science, Basic Energy Sciences, under Awards No. DE-SC0001137 and No. DE-SC0019394, as part of the CCS and CTC Programs. V.S. gratefully acknowledges support from the U.S. Department of Energy through the LANL/LDRD Program and the Center for Non-Linear Studies for part of this work. The authors thank Stony Brook Research Computing and Cyberinfrastructure, and the Institute for Advanced Computational Science at Stony Brook University for access to the high-performance Sea-Wulf computing system, which was made possible by a \$1.4 million National Science Foundation Grant No. 1531492. B.P. acknowledges the National Science Foundation [Platform for the Accelerated Realization, Analysis, and Discovery of Interface Materials (PARADIM)] under Cooperative Agreement No. DMR-2039380. C.E.D. acknowledges support from the National Science Foundation under Grant No. DMR-1918455. The Flatiron Institute is a division of the Simons Foundation.

APPENDIX A: BAND ALIGNMENT

Our current work focuses on a qualitative understanding of the energy level alignment for different (001) SrTiO₃ surface terminations in conjunction with vacuum and water. All calculations are spin polarized, and the GGA + *U* computations included a Hubbard *U* correction term of 4.45 eV for the Ti 3*d* states [55]. The (001) SrTiO₃ surface calculations are performed with 13 layer surface slabs for both the vacuum-interfacing symmetric SrO- and TiO₂-terminated structures, as shown in Fig. S5 within the Supplemental Material [48]. A vacuum region of 15 Å (along the *z* axis) is found to be sufficient to separate the two nonpolar surfaces of a symmetric SrTiO₃ slab. The structures used for determining the band-edge positions in Fig. 5 are geometrically relaxed until the remnant forces in the system are less than 0.01 eV/Å. While a

large set of simulations in this work are performed with a computationally efficient GGA-type exchange-correlation functional, the sensitivity of band-related properties to the hierarchy of functional [66] used is widely recognized [51,54]. Hence, we estimate the band-edge positions using a range-separated hybrid functional, HSE06 [57,58], as implemented in VASP [67]. A plane-wave cutoff of 500 eV is used with the projector augmented-wave (PAW) method of potentials [68] in VASP and the reciprocal space is sampled with a single k point at Γ . This allows for a more accurate quantitative comparison of the energy levels. Extended results obtained with DFT + U are presented in the Supplemental Material [48] (see Fig. S4). These results also include level alignments for slabs solvated with a single monolayer of water.

The band edges for SrTiO₃/vacuum slabs are determined using a surface-vacuum alignment technique in which the VBE is given by the difference between the vacuum level derived from the electrostatic potential of the slab model and the highest occupied level (HOMO) in the system. Similarly, the conduction band edge is given by the difference between the vacuum level and the lowest unoccupied energy level (LUMO) of the slab. The band alignments for the symmetric terminations of SrO/vacuum and TiO₂/vacuum are given in Sec. S2 of the Supplemental Material [48].

For the fully solvated SrTiO₃/H₂O interfaces, we obtain the position of the $1b_1$ peak, which marks the highest occupied state in the bulk region of water and reference it to the vacuum obtained from a pure water-slab calculation. This amounts to an energy shift of the kind $(E_{1b_1,\text{bulk}})_{\text{STO/water}} \rightarrow (E_{1b_1})_{\text{water slab}}$. The band-edge energy (HOMO and LUMO) levels of the full SrTiO₃/H₂O system are then aligned with respect to the $1b_1$ level of water. In the absence of an exact “vacuum level” in the case of solvated SrTiO₃ surfaces, the $1b_1$ level serves as a natural datum against which the band energies can be compared. A detailed account of the band alignment in SrTiO₃/water surfaces is given in Sec. S4 of the Supplemental Material [48].

APPENDIX B: MODELING OF PHOTOCATALYTIC WATER OXIDATION

We consider several SrO- and TiO₂-terminated water oxidation sites and the associated redox potentials are reported in Tables S1 and S2 within the Supplemental Material [48]. In our *ab initio* simulations, we do not explicitly model a photon adsorption event or the photo-generated charge carrier separation. We assume that the hole, while being generated in the bulk of the catalyst (SrTiO₃), becomes available at the top of the valence band to oxidize water and release oxygen. At each step of our proposed water oxidation mechanism, one is given to understand that an electron is removed from the active site region (in our case, the SrTiO₃ slab) filling a photohole

generated in the aqueous reservoir. While the charge transfer phenomenon at the intersection of the SrTiO₃ slab and physisorbed water is of primary interest, we find that the interaction between surface-dissociated water species and the remainder bulk solvent plays a crucial mechanistic role too. Hence, in this study, we go beyond the implicit-solvent model of Shen *et al.* [34] and explicitly consider all of the water molecules in the solvated SrTiO₃ system. The presence of bulk water beyond the first adsorbed monolayer at the catalyst surface acts as a reservoir for coupling the loss of a proton with an oxidation event.

From a single equilibrated MD trajectory, we select a snapshot such as Fig. 6(a)(i), and evaluate the completion of the proposed cycle. Following this, at each PCET step, a proton and an electron (that is, a hydrogen atom) are removed from either a hydroxide ion dissociated on the SrTiO₃ surface or a water molecule that is hydrogen bonded to the target surface intermediate. As the geometric optimization of each intermediate structure is carried out at $T = 0$ K, the temperature effects are not considered explicitly; however, the initial structure of a PCET cycle is always derived from a thermostated parent trajectory. Apart from considering a fully solvated periodic system, our calculations of free energy changes and standard reduction potentials follow a similar procedure as outlined in a previous work by Shen *et al.* [34].

In addition, we allow for a complete relaxation of the solvent in the system, and after each proton removal, we observe that the water molecules near the active site rearrange to initiate the following reaction in the cycle. We also note that, despite using a semilocal exchange and correlation (XC) potential, namely vdW BH [69], the localization of the photohole on the initial reaction species is, in fact, independent of the XC potential [70]. We also confirmed that systems (i) and (iii) in Fig. 6(a) are singlets and systems (ii) and (iv) are electronic doublets.

1. Gibbs free energy and standard reduction potentials

The standard redox potentials are computed with respect to the NHE. As a photocatalyst, SrTiO₃ supplies an over-potential defined in this case as the difference between VBE and NHE [71,72]. The standard free energy for the one-electron hydrogen oxidation reaction at NHE is given by

$$\Delta G_{\text{NHE}} = G_s(\text{H}^+) + G_g(e^-) - \frac{G_g(\text{H}_2)}{2}, \quad (\text{B1})$$

$$G_s(\text{H}^+) = G_g(\text{H}^+) + \Delta G_{\text{solv.}}(\text{H}^+),$$

where $G_g(\text{H}_2) = -31.386$ eV is the standard free energy of a gas-phase H₂ molecule computed using methods consistent with the other calculations in this work. The standard free energy $G_g(\text{H}_2)$ also contains the contribution of vibrational zero-point energies (ZPEs) [73]. The

standard free energy of a gas-phase electron, $G_g(e^-) = -0.0376$ eV, is obtained using the Fermi-Dirac statistics [74]. The standard free energy of a solvated proton, $G_s(H^+) = -11.719$ eV, is computed using the free energy of a gas-phase proton $G_g(H^+)$, and the experimental solvation energy of the proton $\Delta G_{\text{solv.}}(H^+)$ [75,76]. Thus, using Eq. (B1), we obtain the standard oxidation potential of the NHE, $E_{\text{NHE}}^o = -\Delta G_{\text{NHE}} = -3.936$ eV. The Gibbs free energy change computed at each step of the PCET cycle (ΔG_I) includes the ZPEs of the respective reaction intermediates. On the absolute scale,

$$\begin{aligned} \Delta G_{\text{abs},1} &= G(ii) - G(i) - E_{\text{ZPE}}(\text{OH}^-) \\ &\quad + G_s(H^+) + G_g(e^-), \\ \Delta G_{\text{abs},2} &= G(iii) - G(ii) + E_{\text{ZPE}}(\text{OOH}^-) - E_{\text{ZPE}}(\text{H}_2\text{O}) \\ &\quad + G_s(H^+) + G_g(e^-), \\ \Delta G_{\text{abs},3} &= G(iv) - G(iii) + E_{\text{ZPE}}(\text{O}_2^{\bullet-}) - E_{\text{ZPE}}(\text{OOH}^-) \\ &\quad + G_s(H^+) + G_g(e^-), \\ \Delta G_{\text{abs},4} &= G(v) - G(iv) + E_{\text{ZPE}}(\text{OH}^-) + E_{\text{ZPE}}(\text{O}_2) \\ &\quad - E_{\text{ZPE}}(\text{O}_2^{\bullet-}) - E_{\text{ZPE}}(\text{H}_2\text{O}) + G_s(H^+) \\ &\quad + G_g(e^-), \end{aligned} \quad (\text{B2})$$

where the successive PCET steps differ in one proton and electron ($H^+ + e^-$) pair, and the second and fourth steps borrow a H_2O molecule from the interacting bulk water reservoir. On the physical (NHE) scale, the Gibbs free energy changes and the standard one-electron reduction potentials translate to $\Delta G_I = E^o = \Delta G_{\text{abs},I} - \Delta G_{\text{NHE}}$. A detailed description of the water oxidation PCET mechanism and the band alignment at the interface of $\text{SrTiO}_3/\text{water}$ can be found in the Supplemental Material [48] and Ref. [77].

Input files and Jupyter notebooks outlining various calculations are provided in a data repository associated with this manuscript [78].

-
- [1] A. Kudo, and Y. Miseki, Heterogeneous photocatalyst materials for water splitting, *Chem. Soc. Rev.* **38**, 253 (2009).
 - [2] K. Maeda, and K. Domen, New non-oxide photocatalysts designed for overall water splitting under visible light, *J. Phys. Chem. C* **111**, 7851 (2007).
 - [3] R. Rousseau, V.-A. Glezakou, and A. Selloni, Theoretical insights into the surface physics and chemistry of redox-active oxides, *Nat. Rev. Mater.* **5**, 460 (2020).
 - [4] A. L. Linsebigler, G. Lu, and J. T. Yates, Photocatalysis on TiO_2 surfaces: Principles, mechanisms, and selected results, *Chem. Rev.* **95**, 735 (1995).

- [5] H. Eidsvåg, S. Bentouba, P. Vajeeston, S. Yohi, and D. Velauthapillai, TiO_2 as a photocatalyst for water splitting—an experimental and theoretical review, *Molecules* **26**, 1687 (2021).
- [6] A. Miyoshi, S. Nishioka, and K. Maeda, Water splitting on rutile TiO_2 -based photocatalysts, *Chem. Eur. J.* **24**, 18204 (2018).
- [7] K. Rajeshwar, Hydrogen generation at irradiated oxide semiconductor–solution interfaces, *J. Appl. Electrochem.* **37**, 765 (2007).
- [8] D. Lee, W. Wang, C. Zhou, X. Tong, M. Liu, G. Galli, and K.-S. Choi, The impact of surface composition on the interfacial energetics and photoelectrochemical properties of BiVO_4 , *Nat. Energy* **6**, 287 (2021).
- [9] P. Kanhere, and Z. Chen, A review on visible light active perovskite-based photocatalysts, *Molecules* **19**, 19995 (2014).
- [10] R. Li, F. Zhang, D. Wang, J. Yang, M. Li, J. Zhu, X. Zhou, H. Han, and C. Li, Spatial separation of photogenerated electrons and holes among {010} and {110} crystal facets of BiVO_4 , *Nat. Commun.* **4**, 1432 (2013).
- [11] M. S. Wrighton, A. B. Ellis, P. T. Wolczanski, D. L. Morse, H. B. Abrahamson, and D. S. Ginley, Strontium titanate photoelectrodes, efficient photoassisted electrolysis of water at zero applied potential, *J. Am. Chem. Soc.* **98**, 2774 (1976).
- [12] K. van Benthem, C. Elsässer, and R. H. French, Bulk electronic structure of SrTiO_3 : Experiment and theory, *J. Appl. Phys.* **90**, 6156 (2001).
- [13] J. L. Giocondi, and G. S. Rohrer, Structure sensitivity of photochemical oxidation and reduction reactions on SrTiO_3 surfaces, *J. Am. Ceram. Soc.* **86**, 1182 (2003).
- [14] H. Kato, M. Kobayashi, M. Hara, and M. Kakihana, Fabrication of SrTiO_3 exposing characteristic facets using molten salt flux and improvement of photocatalytic activity for water splitting, *Catal. Sci. Technol.* **3**, 1733 (2013).
- [15] H. Kato, and A. Kudo, Visible-light-response and photocatalytic activities of TiO_2 and SrTiO_3 photocatalysts codoped with antimony and chromium, *J. Phys. Chem. B* **106**, 5029 (2002).
- [16] D. Wang, J. Ye, T. Kako, and T. Kimura, Photophysical and photocatalytic properties of SrTiO_3 doped with Cr cations on different sites, *J. Phys. Chem. B* **110**, 15824 (2006).
- [17] W. Wei, Y. Dai, H. Jin, and B. Huang, Density functional characterization of the electronic structure and optical properties of Cr-doped SrTiO_3 , *J. Phys. D: Appl. Phys.* **42**, 055401 (2009).
- [18] R. Niishiro, H. Kato, and A. Kudo, Nickel and either tantalum or niobium-codoped TiO_2 and SrTiO_3 photocatalysts with visible-light response for H_2 or O_2 evolution from aqueous solutions, *Phys. Chem. Chem. Phys.* **7**, 2241 (2005).
- [19] R. Konta, T. Ishii, H. Kato, and A. Kudo, Photocatalytic activities of noble metal ion doped SrTiO_3 under visible light irradiation, *J. Phys. Chem. B* **108**, 8992 (2004).
- [20] T. Ohsawa, K. Nakajima, Y. Matsumoto, and H. Koinuma, Combinatorial discovery of anomalous substrate effect on the photochemical properties of transition metal-doped epitaxial SrTiO_3 heterostructures, *Appl. Surf. Sci.* **252**, 2603 (2006), proceedings of the Third Japan-US Workshop on Combinatorial Material Science and Technology.

- [21] R. Tanaka, S. Takata, M. Katayama, R. Takahashi, J. K. Grepstad, T. Tybell, and Y. Matsumoto, Photocatalytic synthesis of silver-oxide clathrate Ag₇O₈NO₃, *J. Electrochem. Soc.* **157**, E181 (2010).
- [22] D. Wang, T. Kako, and J. Ye, New series of solid-solution semiconductors (AgNbO₃)_{1-x}(SrTiO₃)_x with modulated band structure and enhanced visible-light photocatalytic activity, *J. Phys. Chem. C* **113**, 3785 (2009).
- [23] V. Subramanian, R. K. Roeder, and E. E. Wolf, Synthesis and UV-visible-light photoactivity of noble-metal-SrTiO₃ composites, *Ind. Eng. Chem. Res.* **45**, 2187 (2006).
- [24] M. Plaza, X. Huang, J. Y. P. Ko, M. Shen, B. H. Simpson, J. Rodríguez-López, N. L. Ritzert, K. Letchworth-Weaver, D. Gunceler, D. G. Schlom, T. A. Arias, J. D. Brock, and H. D. Abruña, Structure of the photo-catalytically active surface of SrTiO₃, *J. Am. Chem. Soc.* **138**, 7816 (2016).
- [25] Y. Xiong, and I. Dabo, Influence of surface restructuring on the activity of SrTiO₃ photoelectrodes for photocatalytic hydrogen reduction, *Phys. Rev. Mater.* **3**, 065801 (2019).
- [26] R. Asai, H. Nemoto, Q. Jia, K. Saito, A. Iwase, and A. Kudo, A visible light responsive rhodium and antimony-codoped SrTiO₃ powdered photocatalyst loaded with an IrO₂ cocatalyst for solar water splitting, *Chem. Commun.* **50**, 2543 (2014).
- [27] K. Furuhashi, Q. Jia, A. Kudo, and H. Onishi, Time-resolved infrared absorption study of SrTiO₃ photocatalysts codoped with rhodium and antimony, *J. Phys. Chem. C* **117**, 19101 (2013).
- [28] J. Jiang, K. Kato, H. Fujimori, A. Yamakata, and Y. Sakata, Investigation on the highly active SrTiO₃ photocatalyst toward overall H₂O splitting by doping Na ion, *J. Catal.* **390**, 81 (2020).
- [29] Y. Zhu, P. A. Salvador, and G. S. Rohrer, Controlling the relative areas of photocathodic and photoanodic terraces on the SrTiO₃(111) surface, *Chem. Mater.* **28**, 5155 (2016).
- [30] M. Zhang, P. A. Salvador, and G. S. Rohrer, Influence of pH and surface orientation on the photochemical reactivity of SrTiO₃, *ACS Appl. Mater. Interfaces* **12**, 23617 (2020).
- [31] S. Su, I. Siretanu, D. van den Ende, B. Mei, G. Mul, and F. Mugele, Facet-dependent surface charge and hydration of semiconducting nanoparticles at variable pH, *Adv. Mater.* **33**, 2106229 (2021).
- [32] A. M. Schultz, Y. Zhang, P. A. Salvador, and G. S. Rohrer, Effect of crystal and domain orientation on the visible-light photochemical reduction of Ag on BiFeO₃, *ACS Appl. Mater. Interfaces* **3**, 1562 (2011).
- [33] Y. Ham, T. Hisatomi, Y. Goto, Y. Moriya, Y. Sakata, A. Yamakata, J. Kubota, and K. Domen, Flux-mediated doping of SrTiO₃ photocatalysts for efficient overall water splitting, *J. Mater. Chem. A* **4**, 3027 (2016).
- [34] X. Shen, Y. A. Small, J. Wang, P. B. Allen, M. V. Fernández-Serra, M. S. Hybertsen, and J. T. Muckerman, Photocatalytic water oxidation at the GaN (10 $\bar{1}$ 0)-water interface, *J. Phys. Chem. C* **114**, 13695 (2010).
- [35] S. Selcuk, and A. Selloni, Facet-dependent trapping and dynamics of excess electrons at anatase TiO₂ surfaces and aqueous interfaces, *Nat. Mater.* **15**, 1107 (2016).
- [36] M. Crespillo, J. Graham, F. Agulló-López, Y. Zhang, and W. Weber, Recent advances on carrier and exciton self-trapping in strontium titanate: Understanding the luminescence emissions, *Crystals* **9**, 95 (2019).
- [37] M. Kawasaki, K. Takahashi, T. Maeda, R. Tsuchiya, M. Shinohara, O. Ishiyama, T. Yonezawa, M. Yoshimoto, and H. Koinuma, Atomic control of the SrTiO₃ crystal surface, *Science* **266**, 1540 (1994).
- [38] G. Koster, B. L. Kropman, G. J. Rijnders, D. H. Blank, and H. Rogalla, Quasi-ideal strontium titanate crystal surfaces through formation of strontium hydroxide, *Appl. Phys. Lett.* **73**, 2920 (1998).
- [39] T. Ohnishi, K. Shibuya, M. Lippmaa, D. Kobayashi, H. Kumigashira, M. Oshima, and H. Koinuma, Preparation of thermally stable TiO₂-terminated SrTiO₃ (100) substrate surfaces, *Appl. Phys. Lett.* **85**, 272 (2004).
- [40] A. Gura, G. Bertino, B. Bein, and M. Dawber, Transition regime from step-flow to step-bunching in the growth of epitaxial SrRuO₃ on (001) SrTiO₃, *Appl. Phys. Lett.* **112**, 182902 (2018).
- [41] A. Biswas, C.-H. Yang, R. Ramesh, and Y. H. Jeong, Atomically flat single terminated oxide substrate surfaces, *Prog. Surf. Sci.* **92**, 117 (2017).
- [42] I. Velasco-Davalos, R. Thomas, and A. Ruediger, Realization of single-termination SrTiO₃ (100) surfaces by a microwave-induced hydrothermal process, *Appl. Phys. Lett.* **103**, 202905 (2013).
- [43] S. Chambers, T. Droubay, C. Capan, and G. Sun, Unintentional F doping of SrTiO₃(001) etched in HF acid-structure and electronic properties, *Surf. Sci.* **606**, 554 (2012).
- [44] R. Bachelet, F. Sánchez, F. J. Palomares, C. Ocal, and J. Fontcuberta, Atomically flat SrO-terminated SrTiO₃(001) substrate, *Appl. Phys. Lett.* **95**, 141915 (2009).
- [45] D. Tiwari, and S. Dunn, Photochemistry on a polarisable semi-conductor: What do we understand today?, *J. Mater. Sci.* **44**, 5063 (2009).
- [46] K. Szot, and W. Speier, Surfaces of reduced and oxidized SrTiO₃ from atomic force microscopy, *Phys. Rev. B* **60**, 5909 (1999).
- [47] R. Bachelet, F. Sánchez, J. Santiso, C. Munuera, C. Ocal, and J. Fontcuberta, Self-assembly of SrTiO₃ (001) chemical-terminations: A route for oxide-nanostructure fabrication by selective growth, *Chem. Mater.* **21**, 2494 (2009).
- [48] See Supplemental Material at <http://link.aps.org/supplemental/10.1103/PRXEnergy.1.023002> for details on band alignment and proton-coupled electron transfer.
- [49] N. Domingo, E. Pach, K. Cordero-Edwards, V. Pérez-Dieste, C. Escudero, and A. Verdaguer, Water adsorption, dissociation and oxidation on SrTiO₃ and ferroelectric surfaces revealed by ambient pressure X-ray photoelectron spectroscopy, *Phys. Chem. Chem. Phys.* **21**, 4920 (2019).
- [50] J. Wang, L. S. Pedroza, A. Poissier, and M. V. Fernández-Serra, Water dissociation at the GaN(1010) surface: Structure, dynamics and surface acidity, *J. Phys. Chem. C* **116**, 14382 (2012).
- [51] N. Kharche, J. T. Muckerman, and M. S. Hybertsen, First-Principles Approach to Calculating Energy Level Alignment at Aqueous Semiconductor Interfaces, *Phys. Rev. Lett.* **113**, 176802 (2014).
- [52] Z. Zhong, and P. Hansmann, Tuning the work function in transition metal oxides and their heterostructures, *Phys. Rev. B* **93**, 235116 (2016).

- [53] H.-J. Sung, Y. Mochizuki, and F. Oba, Surface reconstruction and band alignment of nonmetallic $A(II)B(IV)O_3$ perovskites, *Phys. Rev. Mater.* **4**, 044606 (2020).
- [54] T. Ma, R. Jacobs, J. Booske, and D. Morgan, Understanding the interplay of surface structure and work function in oxides: A case study on $SrTiO_3$, *APL Mater.* **8**, 071110 (2020).
- [55] C. Ricca, I. Timrov, M. Cococcioni, N. Marzari, and U. Aschauer, Self-consistent DFT + U + V study of oxygen vacancies in $SrTiO_3$, *Phys. Rev. Res.* **2**, 023313 (2020).
- [56] T. W. Kim, Y. Ping, G. A. Galli, and K.-S. Choi, Simultaneous enhancements in photon absorption and charge transport of bismuth vanadate photoanodes for solar water splitting, *Nat. Commun.* **6**, 8769 (2015).
- [57] J. Heyd, G. E. Scuseria, and M. Ernzerhof, Hybrid functionals based on a screened Coulomb potential, *J. Chem. Phys.* **118**, 8207 (2003).
- [58] J. Heyd, G. E. Scuseria, and M. Ernzerhof, Erratum: "Hybrid functionals based on a screened Coulomb potential" [*J. Chem. Phys.* **118**, 8207 (2003)], *J. Chem. Phys.* **124**, 219906 (2006).
- [59] L. Li, J. T. Muckerman, M. S. Hybertsen, and P. B. Allen, Phase diagram, structure, and electronic properties of $(Ga_{1-x}Zn_x)(N_{1-x}O_x)$ solid solutions from DFT-based simulations, *Phys. Rev. B* **83**, 134202 (2011).
- [60] S. Hammes-Schiffer, and G. Galli, Integration of theory and experiment in the modelling of heterogeneous electrocatalysis, *Nat. Energy* **6**, 700 (2021).
- [61] S. E. Reyes-Lillo, T. Rangel, F. Bruneval, and J. B. Neaton, Effects of quantum confinement on excited state properties of $SrTiO_3$ from ab initio many-body perturbation theory, *Phys. Rev. B* **94**, 041107(R) (2016).
- [62] J. L. Giocondi, P. A. Salvador, and G. S. Rohrer, The origin of photochemical anisotropy in $SrTiO_3$, *Top. Catal.* **44**, 529 (2007).
- [63] L. Mu, Y. Zhao, A. Li, S. Wang, Z. Wang, J. Yang, Y. Wang, T. Liu, R. Chen, and J. Zhu *et al.*, Enhancing charge separation on high symmetry $SrTiO_3$ exposed with anisotropic facets for photocatalytic water splitting, *Energy Environ. Sci.* **9**, 2463 (2016).
- [64] T. Takata, J. Jiang, Y. Sakata, M. Nakabayashi, N. Shibata, V. Nandal, K. Seki, T. Hisatomi, and K. Domen, Photocatalytic water splitting with a quantum efficiency of almost unity, *Nature* **581**, 411 (2020).
- [65] M. Zhang, P. A. Salvador, and G. S. Rohrer, Influence of pH and surface orientation on the photochemical reactivity of $SrTiO_3$, *ACS Appl. Mater. Interfaces* **12**, 23617 (2020).
- [66] R. Car, Fixing Jacob's ladder, *Nat. Chem.* **8**, 820 (2016).
- [67] G. Kresse and J. Furthmüller, Efficient iterative schemes for ab initio total-energy calculations using a plane-wave basis set, *Phys. Rev. B* **54**, 11169 (1996).
- [68] P. E. Blöchl, Projector augmented-wave method, *Phys. Rev. B* **50**, 17953 (1994).
- [69] K. Berland and P. Hyldgaard, Exchange functional that tests the robustness of the plasmon description of the van der Waals density functional, *Phys. Rev. B* **89**, 035412 (2014).
- [70] V. Sharma and M. Fernández-Serra, Proton-transfer dynamics in ionized water chains using real-time time-dependent density functional theory, *Phys. Rev. Res.* **2**, 043082 (2020).
- [71] K. Takanabe, Photocatalytic water splitting: Quantitative approaches toward photocatalyst by design, *ACS Catal.* **7**, 8006 (2017).
- [72] J. Li and N. Wu, Semiconductor-based photocatalysts and photoelectrochemical cells for solar fuel generation: A review, *Catal. Sci. Technol.* **5**, 1360 (2015).
- [73] R. D. J. III, NIST Computational Chemistry Comparison and Benchmark Database (2020).
- [74] J. E. Bartmess, Thermodynamics of the electron and the proton, *J. Phys. Chem.* **98**, 6420 (1994).
- [75] D. A. McQuarrie, *Statistical Mechanics*, Harper's Chemistry Series (Harper & Row, New York, 1975).
- [76] M. D. Tissandier, K. A. Cowen, W. Y. Feng, E. Gundlach, M. H. Cohen, A. D. Earhart, J. V. Coe, and T. R. Tuttle, The proton's absolute aqueous enthalpy and Gibbs free energy of solvation from cluster-ion solvation data, *J. Phys. Chem. A* **102**, 7787 (1998).
- [77] V. Sharma, Ph.D. Thesis, 2021, <https://www.proquest.com/openview/852f3768f49905a5d3c0c5e85036220a>.
- [78] Zenodo data repository, <https://doi.org/10.5281/zenodo.5838976>.